ChemComm

COMMUNICATION

View Article Online
View Journal

Cite this: DOI: 10.1039/d0cc07268k

Received 3rd November 2020,
Accepted 3rd December 2020

DOI: 10.1039/d0cc07268k

rsc.li/chemcomm

A novel electrochemical biosensor for ultrasensitive Hg^{2+} detection *via* a triple signal amplification strategy†

Wang He,[a] Bin Qiao,[b] Fengzhen Li,[a] Lisha Pan,[a] Delun Chen,[ab] Yang Cao,[ac] Jinchun Tu,[a] Xiaohong Wang,*[a] Chuanzhu Lv*[d] and Qiang Wu*[b]

We developed a novel electrochemical biosensor for ultrasensitive Hg^{2+} detection *via* a triple signal amplification strategy of a DNA dual cycle, organic–inorganic hybrid nanoflowers ($Cu_3(PO_4)_2$ HNFs) and gold nanoparticle (AuNP) probe. The DNA dual cycle was triggered by exonuclease III (Exo III) in the presence of Hg^{2+}, and $Cu_3(PO_4)_2$ HNFs were synthesized as an AuNP probe carrier. The electrochemical biosensor displayed high stability, high sensitivity and excellent specificity, which was improved by up to seven orders of magnitude compared to the World Health Organization (WHO) allowed Hg^{2+} levels in drinking water. This signal amplification strategy could be easily modified and extended to detect other hazardous heavy metals and nucleic acids.

Environmental safety has always been a concern to people. Mercury as one of the most widely used hazardous heavy metals can cause great damage to living organisms at very low concentrations.[1–3] The maximum allowable concentration of Hg^{2+} in drinking water is 2 ppb (10 nM) according to the World Health Organization (WHO).[4,5] The accumulation of mercury ions in the body causes severe damage to organs.[6,7] Therefore, it is important to develop a sensitive method for detecting Hg^{2+} to protect the environment and human health.

Many traditional methods have been applied for monitoring Hg^{2+}, including inductively coupled plasma mass spectrometry,[8] oxidation reduction potential measurements[9] and atomic absorption/emission spectrometry.[10] However, these traditional methods require time-consuming sample pretreatment, sophisticated equipment and trained personnel, making them unsuitable for routine monitoring. To solve these problems, researchers have developed various alternative methods for Hg^{2+} detection, such as fluorescence analysis,[11–14] photoelectronchemistry[10] and electrochemistry.[15] Among these methods, electrochemical strategies have attracted much interest owing to their simplicity, high sensitivity, fast response and low cost, and have been widely used in biological analysis, clinical detection and environmental monitoring.[16] However, electrochemical strategies for detecting Hg^{2+} are still limited by their low selectivity. Hg^{2+} can make two thymine bases specifically bind to form a stable thymine–Hg^{2+}–thymine (T–Hg^{2+}–T) complex.[17–19] Based on this particular combination, several types of electrochemical biosensors have been designed to detect Hg^{2+} and exhibit high selectivity.[20,21]

To improve the sensitivity, nicking endonuclease[22] and exonuclease III (Exo III)[17] have been introduced for target recycling to realize signal circle amplification.[23–25] Moreover, materials with a high surface area, such as AuNPs,[15,26] carbon nanotubes[27] and graphene oxide[28] have been studied for signal amplification. However, these materials are either expensive or complex to make. Therefore, a simple and cheap material is urgently needed. Ge used Cu^{2+} as an inorganic component and a variety of proteins as organic components to synthesize organic–inorganic hybrid nanoflowers ($Cu_3(PO_4)_2$ HNFs).[29] The $Cu_3(PO_4)_2$ HNFs were synthesized simply without using any hazardous reagents and displayed high surface area, good stability and greatly enhanced catalytic activity.[30] The material has been applied in nanocatalysis, enzyme reaction and proteomic analysis. Subsequently, $Cu_3(PO_4)_2$ HNFs can be used in Hg^{2+} sensitive detection systems.

[a] State Key Laboratory of Marine Resource Utilization in South China Sea, Hainan University, Haikou, 570228, China. E-mail: wangxiaohong@hainu.edu.cn; Fax: +86 898 66259764; Tel: +86 898 66259764

[b] School of Tropical Medicine and Laboratory Medicine, Key Laboratory of Emergency and Trauma of Ministry of Education, Research Unit of Island Emergency Medicine, Chinese Academy of Medical Sciences (No. 2019RU013), Hainan Medical University, Haikou, 571199, China. E-mail: wuqiang001001@aliyun.com; Fax: 898 66984599; Tel: +86 898 66984599

[c] Qiongtai Normal University, Haikou, 571127, China

[d] Department of Emergency, Hainan Clinical Research Center for Acute and Critical Diseases, The Second Affiliated Hospital of Hainan Medical University, Emergency and Trauma College, Hainan Medical University, Haikou, 571199, China. E-mail: lvchuanzhu677@126.com; Fax: +86 898 66989196; Tel: +86 898 66989196

† Electronic supplementary information (ESI) available: Experimental section; EDX analyses and XPS survey spectra of c-probe/AuNPs/$Cu_3(PO_4)_2$ HNFs; UV-vis absorbance spectrum of AuNPs and R-probe/AuNPs; optimization of assay conditions; recovery experiments of Hg^{2+} in drinking water; comparison of different Hg^{2+} detection methods based on T–Hg^{2+}–T; selectivity of biosensor sequences for nucleic acids used in this study. See DOI: 10.1039/d0cc07268k

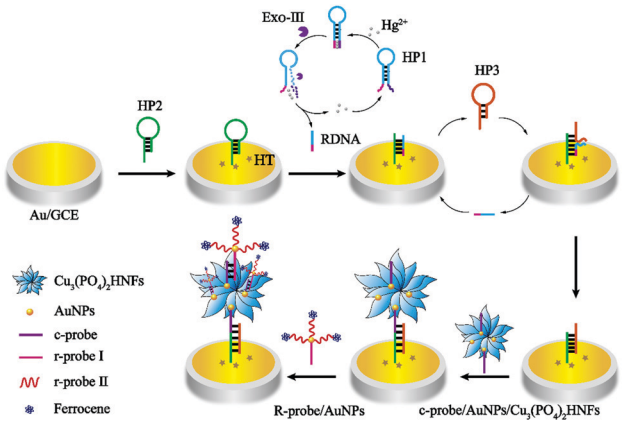

Scheme 1 Schematic of the preparation of an electrochemical biosensor for Hg^{2+} detection based on triple signal amplification.

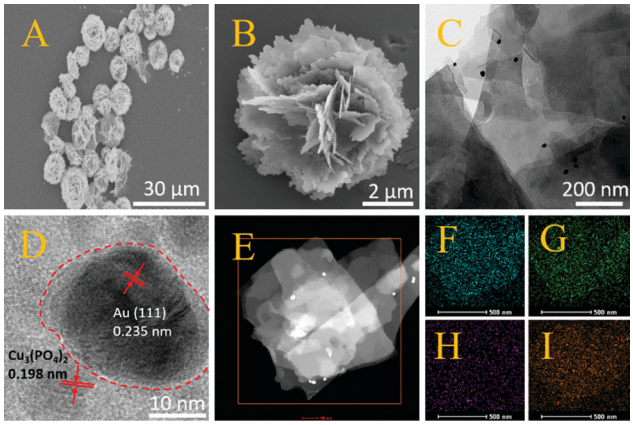

Fig. 1 (A and B) SEM images and (C) TEM images of the c-probe/AuNPs/$Cu_3(PO_4)_2$ HNFs; (D) HRTEM image and SAED pattern of the c-probe/AuNPs/$Cu_3(PO_4)_2$ HNFs; (E) HAADF-STEM image and (F–I) STEM-EDX mapping analyses of the c-probe/AuNPs/$Cu_3(PO_4)_2$ HNFs.

Herein, we report a novel Hg^{2+} detection electrochemical biosensor based on the triple signal amplification strategy of a DNA dual cycle, $Cu_3(PO_4)_2$ HNFs and a AuNP probe. As shown in Scheme 1. The first strategy of the DNA dual cycle amplification was triggered by Exo III to digest the thymine base rich (T-rich) DNA formed through T–Hg^{2+}–T coordination to release Hg^{2+} for the next cycle. Simultaneously, large amounts of report DNA (RDNA) were released to form a new double stranded DNA (dsDNA) structure with hairpin 2 (HP2) on the electrode. Subsequently, the introduction of hairpin 3 (HP3) opened the new dsDNA to release RDNA again for the next cycle. After the DNA dual cycle amplification, the special probe was eventually formed on the electrode. $Cu_3(PO_4)_2$ HNFs were synthesized *via* a facile green synthetic method. AuNPs labeled with the c-probe were effectively anchored on the $Cu_3(PO_4)_2$ HNFs (c-probe/AuNPs/$Cu_3(PO_4)_2$ HNFs), thus improving the distribution homogeneity of the AuNPs and improving their efficiency. Then, the c-probe/AuNPs/$Cu_3(PO_4)_2$ HNFs were connected to the probe on the electrode. Finally, AuNPs modified with r-probe (r-probe 1 and r-probe 2 marked with ferrocene) were connected by the c-probe on the $Cu_3(PO_4)_2$ HNFs, resulting in further electrochemical signal amplification. The results suggest that the proposed electrochemical biosensor displays remarkable amplification efficiency, rapid response, and high sensitivity and selectivity for the detection of Hg^{2+}. This strategy was successfully applied to detect Hg^{2+} in spiked water samples.

The morphology and size of the c-probe/AuNPs/$Cu_3(PO_4)_2$ HNFs was characterized *via* scanning electron microscopy (SEM) and transmission electron microscopy (TEM). As shown in Fig. 1A and B, the synthesized sample displays a flower-like nanostructure with high uniformity and good dispersion. The size of the nanocomposites was 7 ± 1.5 μm. The TEM image reveals that the AuNPs were successfully loaded on the nanomaterials (Fig. 1C). As shown in Fig. 1D, the AuNPs are small particles with a diameter of approximately 20 nm that are scattered on the surface of the nanomaterials. The selected area electron diffraction (SAED) pattern in Fig. S1 (ESI†) confirms that the composite material has a polycrystalline structure. The high-angle annular dark-field-scanning transmission electron microscopy (HAADF-STEM) image (Fig. 1E), energy dispersive X-ray (EDX) pattern (Fig. S2, ESI†) and scanning transmission EDX (STEM-EDX) mapping analyses (Fig. 1F–I and Fig. S3, ESI†) demonstrated the presence of Cu, P, O, C, N and Au in the nanomaterials, corresponding to the chemical nature of the material.

Fourier-transform infrared (FT-IR) spectroscopy was employed to further characterize the chemical formation of the c-probe/AuNPs/$Cu_3(PO_4)_2$ HNFs. As shown in Fig. 2A, the FT-IR spectrum of BSA, distinctive absorption peaks occurred at 3445–3296, 3061, 2950–2860, 1655, 1539, and 1242 cm^{-1}, which were attributed to the –OH, amide A (–NH), and C–H, amide I (C═O), amide II (N–H bending and C–N stretching vibrations) and amide III, respectively.[31] In the FT-IR spectrum of $Cu_3(PO_4)_2{\cdot}5H_2O$, the absorption bands at 605 and 1050 cm^{-1} are caused by the bending vibration and asymmetrical stretching of the P–O bond. A strong and wide band at 3421 cm^{-1} corresponds to the asymmetric and symmetric vibrational modes of the O–H bond of the physisorbed H_2O molecules.[32] In comparison with the bands of BSA and $CuSO_4{\cdot}5H_2O$, the FT-IR spectrum of the c-probe/AuNPs/$Cu_3(PO_4)_2$ HNFs exhibits all the characteristic absorption bands of the above mentioned groups. The new peaks at 561, 991 and 1147 cm^{-1} were attributed to the in-plane bending vibration of PO_4^{3-}, symmetric

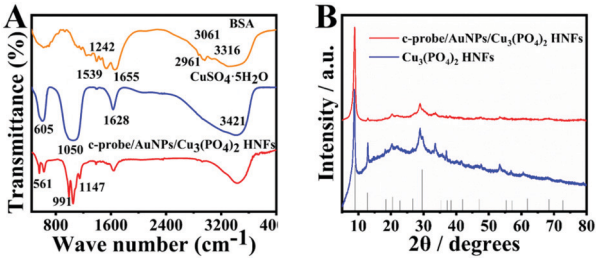

Fig. 2 (A) FT-IR spectra of BSA, $CuSO_4{\cdot}5H_2O$ and the c-probe/AuNPs/$Cu_3(PO_4)_2$ HNFs. (B) XRD pattern of the $Cu_3(PO_4)_2$ HNFs and c-probe/AuNPs/$Cu_3(PO_4)_2$ HNFs.

stretching vibrations of the PO_4^{3-} and asymmetrical stretching of PO_4^{3-}.[31–33] Hence, BSA and the c-probe were assembled into the $Cu_3(PO_4)_2$ HNFs successfully.

The crystalline nature of the c-probe/AuNPs/$Cu_3(PO_4)_2$ HNFs and $Cu_3(PO_4)_2$ HNFs were analyzed by X-ray diffraction (XRD). As shown in Fig. 2B, the positions and relative intensities of all of the diffraction peaks of the $Cu_3(PO_4)_2$ HNFs and the c-probe/AuNPs/$Cu_3(PO_4)_2$ HNFs can be well matched to the standard cards of $Cu_3(PO_4)_2$ (00-022-0548), indicating that the c-probe/AuNPs/$Cu_3(PO_4)_2$ HNFs were well crystallized.

The stepwise fabrication process of the proposed biosensor was monitored *via* cyclic voltammetry (CV), as shown in Fig. 3A. Compared with the low signal of the bare GCE (curve *a*), the oxidation peak current of GCE modified with AuNPs (curve *b*) was significantly enhanced, because the increased active surface area of the AuNPs/GCE accelerated the electron transfer. After incubating HP2 on the AuNPs/GCE, an obvious decrease in the current was observed due to HP2 blocking the electron transfer tunnel (curve *c*). When blocking occurred with HT, the oxidation peak current decreased (curve *d*). After the immobilization of RDNA, the oxidation peak current increased (curve *e*) because the hybridization reaction between HP2 and RDNA reduced the steric hindrance. After incubating with HP3, the peak current decreased again (curve *f*), indicating that the surface of the electrode was modified successfully with HP3.

Electrochemical impedance spectroscopy (EIS) was employed to study the modification process of the electrode surface layers. As shown in Fig. 3B, a small semicircle of the bare GCE (curve *a*) was observed, and after GCE was deposited in $HAuCl_4$ (curve *b*), the electron transfer resistance significantly decreased because the AuNPs enhanced the electrical conductivity. When the electrode was modified with HP2, the impedance value increased (curve *c*). Then, an increased impedance value was observed after dropping HT on the electrode (curve *d*) because the nonspecific binding sites were blocked by HT. Subsequently, the impedance values decreased (curves *e*) upon incubation with RDNA due to the reduced electrostatic repulsion of the oligonucleotide strands and steric hindrance from the stem-loop structures. Finally, the impedance slightly increased after incubating with HP3 (curves *f*), which was ascribed to the immobilized HP3 increasing the thickness of the interface and reducing the effective area. The above results indicate that the electrochemical biosensor was fabricated successfully.

To achieve the best performance of the biosensor, we systematically optimized the effects that the experimental conditions have on the designed biosensor. The concentration of HP1 increased from 1 to 5 μM, and the signal changes (Δi) for Hg^{2+} reached a maximum when the concentration of HP1 increased to 4 μM (Fig. S6A, ESI†). Thus, 4 μM of HP1 was considered to be the optimum incubation concentration. The dosages of the Exo III enzyme and the nicking time substantially influenced the proposed biosensor. The results are shown in Fig. S6B (ESI†). With an increase in the dosages of Exo III, the signal changes (Δi) in the square wave voltammetry (SWV) measurements increased and reached a maximum at 4 U. Therefore, 4 U of Exo III was used in the following experiments. The current signal changes (Δi) gradually increased with an increase in the nicking time of Exo III until a stable value was reached after 60 min (Fig. S6C, ESI†). Hence, 60 min was chosen as the best nicking time for the following study.

The analytical performance of the electrochemical biosensor was investigated under optimized experimental conditions. As shown in Fig. S7 (ESI†), we can see that the peak current was 10.32 μA in the DNA dual cycle. After immobilising the $Cu_3(PO_4)_2$ HNFs, the peak current increased to 15.36 μA. The peak current further increased to 18.41 μA after incubating the AuNP probe. This demonstrated that the current signal was amplified step by step through three amplification strategies. In Fig. 4A, the electrochemical signals of Hg^{2+} at different concentrations in the range of 1 fM to 10 nM were determined. With an increase in the concentration of Hg^{2+}, the response signals of the electrochemical biosensor were enhanced. Fig. S5B (ESI†) shows a highly linear relationship between Δi and the logarithmic concentration of Hg^{2+} ($\lg C$). The regression equation can be represented as Δi (μA) = 14.38293 + 3.23655 $\lg C$ (R^2 = 0.99844) with a limit of detection (LOD) of 0.19 fM, as calculated using the traditional approach.[7]

Compared with other previously reported methods for Hg^{2+} detection, the proposed electrochemical biosensor exhibited better analytical performance (Table S1, ESI†). This electrochemical biosensor displayed a lower LOD and wide linear response range in terms of analytical performance, which can

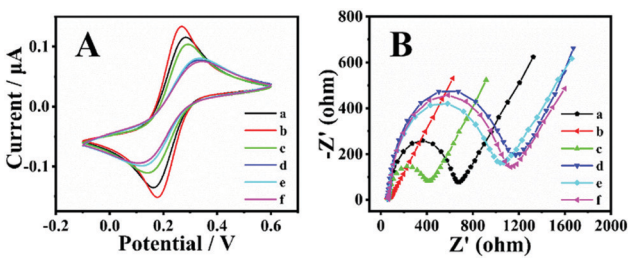

Fig. 3 Signal change of the (A) CV and (B) EIS during the biosensor fabrication process in 5 mM $[Fe(CN)_6]^{3-/4-}$ with 100 mM KCl. From curve *a* to curve *f*: (a) bare GCE, (b) AuNPs/GCE, (c) HP2/AuNPs/GCE, (d) HT/HP2/AuNPs/GCE, (e) RDNA/HT/HP2/AuNPs/GCE and (f) HP3/RDNA/HT/HP2/AuNPs/GCE.

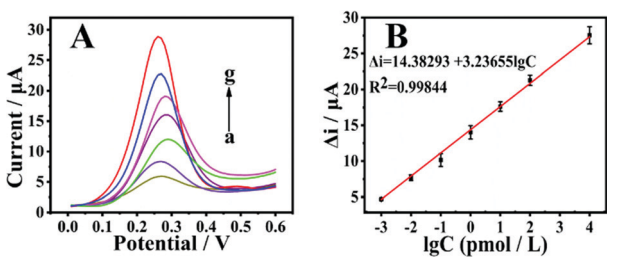

Fig. 4 (A) SWV of the biosensor at different Hg^{2+} concentrations from (a–g) at 1.00 fM, 10.00 fM, 0.10 pM, 1.00 pM, 10.00 pM, 0.10 nM and 10.00 nM. (B) Calibration curve of Δi against the logarithm of the Hg^{2+} concentrations.

be ascribed to the amplification of the mercury ion signal by triple signal amplification.

To investigate the selectivity of the Hg^{2+} assay, we studied the electrochemical current signals in the presence of Cu^{2+}, Ni^{2+}, K^{+}, Fe^{3+}, Pb^{2+}, Co^{2+}, Zn^{2+} and Cd^{2+} using the electrochemical biosensor. The concentrations of Hg^{2+} and other metal ions were 10 pM and 10 nM respectively. Compared to the current response in the presence of Hg^{2+}, the electrochemical response of the biosensor in 10 nM of other interfering metal ions was negligible, and the signal changes (Δi) of the mixture did not display any significant decrease (Fig. S8, ESI†). The results illustrate that our electrochemical biosensor exhibits excellent specificity for Hg^{2+} detection.

To study the feasibility of the electrochemical biosensor for use in practical applications, different concentrations of Hg^{2+} were determined three times using standard addition methods in drinking water samples. The relative standard deviations (RSD) and recovery rates are listed in Table S2 (ESI†), with the results indicating that the RSD was lower than 4.55% and the recoveries are between 94.30% and 106.91%, indicating that the electrochemical biosensor has a potential application for Hg^{2+} detection in actual water samples.

In summary, we demonstrated a novel electrochemical biosensor for ultrasensitive Hg^{2+} detection and signal amplification was achieved *via* the triple signal amplification strategy of a DNA dual cycle, $Cu_3(PO_4)_2$ HNFs and AuNP probe. The prepared $Cu_3(PO_4)_2$ HNFs exhibited a large surface area and high stability and the material was used as a carrier for an AuNP probe. The electrode, $Cu_3(PO_4)_2$ HNFs and AuNP probe were specifically connected by DNA. The sensitivity of the Hg^{2+} detection was greatly enhanced *via* the triple signal amplification strategy. Under optimal conditions, the electrochemical biosensor exhibited a good linear response range from 1 fM to 10 nM with a LOD of 0.19 fM (S/N = 3). This detection limit is approximately eight orders of magnitude more sensitive than the WHO allowed Hg^{2+} levels in drinking water. These findings suggest the potential applications of the biosensor in actual samples. This signal amplification strategy has great potential application for use in the detection of other DNA and RNA targets.

This work was supported by grants from the Finance Science and Technology Project of Hainan Province (ZDYF2019161, 2019RC221), the National Natural Science Foundation of China (51762012, 81860373, 81902154 and 82060386), the CAMS Innovation Fund for Medical Sciences (2019-I2M-5-023) and the Key Laboratory Open Project Fund of Emergency and Trauma of the Ministry of Education (KLET-201910).

Conflicts of interest

There are no conflicts to declare.

Notes and references

1 X. Song, Y. Wang, S. Liu, X. Zhang, H. Wang, J. Wang and J. Huang, *Mikrochim. Acta*, 2019, **186**, 105.
2 Y. Liu, X. Wang and H. Wu, *Biosens. Bioelectron.*, 2017, **87**, 129–135.
3 N. Bi, M. Hu, J. Xu and L. Jia, *Microchim. Acta*, 2017, **184**, 3961–3967.
4 M. Raissy, *Bull. Environ. Contam. Toxicol.*, 2013, **91**, 667–672.
5 Y. Choi, Y. Park, T. Kang and L. P. Lee, *Nat. Nanotechnol.*, 2009, **4**, 742–746.
6 J. Zhao, Y. M. Lei, Y. Q. Chai, R. Yuan and Y. Zhuo, *Biosens. Bioelectron.*, 2016, **86**, 720–727.
7 X. Jiang, H. Wang, H. Wang, R. Yuan and Y. Chai, *Anal. Chem.*, 2016, **88**, 9243–9250.
8 X. Jia, Y. Han, X. Liu, T. Duan and H. Chen, *Spectrochim. Acta, Part B*, 2011, **66**, 88–92.
9 S. Zhang, D. Zhang, X. Zhang, D. Shang, Z. Xue, D. Shan and X. Lu, *Anal. Chem.*, 2017, **89**, 3538–3544.
10 Y. Zhang, M. Yan, J. Jiang, P. Gao, G. Zhang, M. M. F. Choi, C. Dong and S. Shuang, *Sens. Actuators, B*, 2016, **235**, 386–393.
11 T. Rasheed, M. Bilal, F. Nabeel, H. M. N. Iqbal, C. Li and Y. Zhou, *Sci. Total Environ.*, 2018, **615**, 476–485.
12 B. Wang, S. Zhuo, L. Chen and Y. Zhang, *Spectrochim. Acta, Part A*, 2014, **131**, 384–387.
13 H. Xu, X. Zhu, H. Ye, L. Yu, X. Liu and G. Chen, *Chem. Commun.*, 2011, **47**, 12158–12160.
14 J. Zhu, H. Chang, J. J. Li, X. Li and J. W. Zhao, *Spectrochim. Acta, Part A*, 2018, **188**, 170–178.
15 G. Zeng, C. Zhang, D. Huang, C. Lai, L. Tang, Y. Zhou, P. Xu, H. Wang, L. Qin and M. Cheng, *Biosens. Bioelectron.*, 2017, **90**, 542–548.
16 K. Tanabe, Y. Yoshizumi, S. Tsuchiya, R. Y. O. Usuba and H. Suzuki, *Electron. Commun. Jpn*, 2017, **100**, 51–58.
17 S. H. Wu, B. Zhang, F. F. Wang, Z. Z. Mi and J. J. Sun, *Biosens. Bioelectron.*, 2018, **104**, 145–151.
18 X. Song, B. Fu, Y. Lan, Y. Chen, Y. Wei and C. Dong, *Spectrochim. Acta, Part A*, 2018, **204**, 301–307.
19 P. Hou, Y. Long, J. Zhao, J. Wang and F. Zhou, *Spectrochim. Acta, Part A*, 2012, **86**, 76–79.
20 D. Han, Y. R. Kim, J. W. Oh, T. H. Kim, R. K. Mahajan, J. S. Kim and H. Kim, *Analyst*, 2009, **134**, 1857–1862.
21 Y. Lai, Y. Ma, L. Sun, J. Jia, J. Weng, N. Hu, W. Yang and Q. Zhang, *Electrochim. Acta*, 2011, **56**, 3153–3158.
22 M. Q. Hong, M. Y. Wang, J. Wang, X. Q. Xu and Z. Y. Lin, *Biosens. Bioelectron.*, 2017, **94**, 19–23.
23 W. Zhao, M. M. Ali, M. A. Brook and Y. Li, *Angew. Chem., Int. Ed.*, 2008, **47**, 6330–6337.
24 N. C. Seeman, *Nature*, 2003, **421**, 427–431.
25 L. Yan, J. Zhou, Y. Zheng, A. S. Gamson, B. T. Roembke, S. Nakayama and H. O. Sintim, *Mol. BioSyst.*, 2014, **10**, 970–1003.
26 V. Perumal, U. Hashim, S. C. B. Gopinath, R. Haarindraprasad, P. Poopalan, W. W. Liu, M. Ravichandran, S. R. Balakrishnan and A. R. Ruslinda, *Biosens. Bioelectron.*, 2016, **78**, 14–22.
27 Z. Zhu, R. Yang, M. You, X. Zhang, Y. Wu and W. Tan, *Anal. Bioanal. Chem.*, 2010, **396**, 73–83.
28 P. J. Huang and J. Liu, *Chemistry*, 2011, **17**, 5004–5010.
29 J. Ge, J. Lei and R. N. Zare, *Nat. Nanotechnol.*, 2012, **7**, 428–432.
30 L. Xu, Z. Liu, S. Lei, D. Huang, L. Zou and B. Ye, *Microchim. Acta*, 2019, **186**, 473.
31 A. Swaidan, A. Addad, J.-F. Tahon, A. Barras, J. Toufaily, T. Hamieh, S. Szunerits and R. Boukherroub, *Anal. Chim. Acta*, 2020, **1109**, 78–89.
32 Y. Sang, G. Song, Z. Gao, X. Zhang, T. Wang, Y. Li, L. Zhang, Y. Fu and L. Guo, *Nanotechnology*, 2020, **31**, 165504.
33 J. Gao, H. Liu, L. Pang, K. Guo and J. Li, *ACS Appl. Mater. Interfaces*, 2018, **10**, 30441–30450.

